

Stabilizing 459 nm passive optical clock for pumping 1470 nm active optical clock

Haoyang Wu(吴浩洋), Zhiqiang Wen(温智强), Chen Wang(王琛), Zhenfeng Liu(刘珍峰), Jingbiao Chen(陈景标), Shougang Zhang(张首刚), and Deshui Yu(于得水)

Citation: Chin. Phys. B, 2025, 34 (**11**): 114201. DOI: 10.1088/1674-1056/adfefa
http://cpb.iphy.ac.cn; http://iopscience.iop.org/cpb

What follows is a list of articles you may be interested in

Entropy evolution law of a general linear state for diffusion noise

Yingyu Zhang(张映玉) and Yixing Wang(王依兴)
Chin. Phys. B, 2025, 34 (**9**): 094206. DOI: 10.1088/1674-1056/add4f2

Quasi-two-dimensional isotropic laser cooling of atoms for quantum sensing

Xiao Zhang(张孝), Yi Song(宋屹), Yuan Sun(孙远), and Liang Liu(刘亮)
Chin. Phys. B, 2025, 34 (**8**): 084202. DOI: 10.1088/1674-1056/add4f7

Modulation transfer spectroscopy based on acousto-optic modulator with zero frequency shift

Chen-Fei Wu(吴晨菲), Xue-Shu Yan(颜学术), Li-Xun Wei(卫立勋), Pei Ma(马沛), Jian-Hui Tu(涂建辉), Jian-Wei Zhang(张建伟), Li-Jun Wang(王力军)
Chin. Phys. B, 2018, 27 (**11**): 114203. DOI: 10.1088/1674-1056/27/11/114203

Flexible control of semiconductor laser with frequency tunable modulation transfer spectroscopy

Ning Ru(茹宁), Yu Wang(王宇), Hui-Juan Ma(马慧娟), Dong Hu(胡栋), Li Zhang(张力), Shang-Chun Fan(樊尚春)
Chin. Phys. B, 2018, 27 (**7**): 074201. DOI: 10.1088/1674-1056/27/7/074201

Laser frequency stabilization and shifting by usingmodulation transfer spectroscopy

Cheng Bing (程冰), Wang Zhao-Ying (王兆英), Wu Bin (吴彬), Xu Ao-Peng (许翱鹏), Wang Qi-Yu (王启宇), Xu Yun-Fei (徐云飞), Lin Qiang (林强)
Chin. Phys. B, 2014, 23 (**10**): 104222. DOI: 10.1088/1674-1056/23/10/104222

RAPID COMMUNICATION

Stabilizing 459 nm passive optical clock for pumping 1470 nm active optical clock

Haoyang Wu(吴浩洋)[1,2], Zhiqiang Wen(温智强)[1,2], Chen Wang(王琛)[1,†], Zhenfeng Liu(刘珍峰)[3], Jingbiao Chen(陈景标)[4,5], Shougang Zhang(张首刚)[1,2], and Deshui Yu(于得水)[1,6]

[1] *National Time Service Center, Chinese Academy of Sciences, Xi'an* 710600, *China*
[2] *University of Chinese Academy of Sciences, Beijing* 100049, *China*
[3] *Zhejiang Faraday Laser Technology Company Limited, Wenzhou* 325000, *China*
[4] *State Key Laboratory of Photonics and Communications, Institute of Quantum Electronics, School of Electronics, Peking University, Beijing* 100871, *China*
[5] *Hefei National Laboratory, Hefei* 230088, *China*
[6] *Key Laboratory of Time Reference and Applications, Chinese Academy of Sciences, Xi'an* 710600, *China*

(Received 22 June 2025; revised manuscript received 20 August 2025; accepted manuscript online 26 August 2025)

Optical clocks with thermal atoms are characterized by compact size, simple structure, reduced weight, and low power consumption and have the potential for broad out-of-the-lab and commercial applications. Here, we demonstrate a 459 nm optical clock based on the $6S_{1/2}$–$7P_{1/2}$ transition in thermal ^{133}Cs atoms. Two methods, modulation transfer spectroscopy (MTS) and frequency modulation spectroscopy (FMS), are employed to stabilize the frequency of a 459 nm commercial laser to the atomic transition. The MTS-MTS and MTS-FMS beat-note measurements show short-term frequency stabilities of $3.7\times10^{-13}/\sqrt{\tau}$ and $6.4\times10^{-13}/\sqrt{\tau}$, respectively, at the averaging time τ. The 459 nm passive optical clock further serves as the pump for an active 1470 nm optical clock based on the cavityless lasing. The resultant 1470 nm output power reaches over 10 μW and the pump-beam-induced light shift is estimated to be $2\pi\times11$ Hz with a fractional uncertainty of 2.4×10^{-18}. These results demonstrate the feasibility of hybridizing passive and active optical clocks, providing a promising route toward compact multi-wavelength optical frequency standards.

Keywords: modulation transfer spectroscopy, frequency modulation spectroscopy, active optical clocks

PACS: 42.50.–p, 42.62.Fi, 43.58.Hp

DOI: 10.1088/1674-1056/adfefa **CSTR:** 32038.14.CPB.adfefa

1. Introduction

Optical clocks with ultracold ions/atoms have surpassed their microwave counterparts in both stability and accuracy by more than two orders of magnitude,[1,2] paving the way toward the redefinition of the second based on an optical atomic transition.[3] Recent progress, including the millihertz-linewidth ultrastable laser system based on a cryogenic single-crystal silicon cavity,[4] careful evaluation of multi- and hyper-polarizabilities of clock states of ^{87}Sr and ^{171}Yb atoms,[5,6] cancellation of atom–atom interactions,[7] employment of shallow optical lattices,[8] and substantial reduction of the uncertainty of blackbody radiation shifts,[2] have suppressed the systematic uncertainty of optical clocks to below 10^{-18}.[2,9] That is, the clocks would take approximately three times the age of the universe to lose one second. Additionally, the synchronous comparison of optical clocks mitigates the Dick noise, leading to a quantum-projection-noise-limited frequency stability.[10] The unprecedented measurement precision can reach the 10^{-21} level using 10^5 atoms, enabling resolving the gravitational redshift with a millimeter-scale height difference.[11,12] Further, spin squeezing allows for the synchronous comparison beyond the quantum-projection-noise limit, effectively shortening the sampling time for the precise measurement.[13,14] Nevertheless, the high environmental sensitivity and large size of optical clocks with ultracold ions/atoms strongly restrict their applications outside the laboratory.

In contrast, owing to their compact size, reduced weight, and low power consumption, optical clocks with thermal atoms have shown the potential for use in out-of-the-lab environments, though at the cost of the degradation of the clock's stability and accuracy. The spectral linewidth of some commercial laser systems can be much narrower than the natural linewidth of atomic clock transitions, which is at the level of hundreds of kilohertz or a few megahertz. Thus, the pre-stabilization of the clock laser to a high-finesse optical resonator becomes unnecessary, which significantly simplifies the clock structure. In addition, the absence of laser cooling and trapping reduces the number of laser systems that are required for the sample preparation, thereby greatly facilitating the clock operation. Recently, a 1556 nm optical clock based

[†]Corresponding author. E-mail: wangchen@ntsc.ac.cn

© 2025 Chinese Physical Society and IOP Publishing Ltd. All rights, including for text and data mining, AI training, and similar technologies, are reserved.

on the $5S_{1/2}$–$5P_{3/2}$–$5D_{5/2}$ two-photon transition (linewidth of 330 kHz) in thermal rubidium atoms, which features commercialization and deployment, has demonstrated a frequency stability of $4\times10^{-13}/\sqrt{\tau}$.[15] In addition, a 459 nm optical clock based on the modulation transfer spectroscopy (MTS) of the $6S_{1/2}$–$7P_{1/2}$ transition in thermal ^{133}Cs atoms has been reported with a frequency stability of $2.1\times10^{-13}/\sqrt{\tau}$.[16] A MTS-stabilized 532 nm molecular iodine optical clock has shown a frequency stability of 2.5×10^{-14} at $\tau=1$ s.[17] Especially, the MTS between different optical transitions enables a dual-wavelength optical frequency standard based on one quantum ensemble.[18] The further employment of microfabricated vapor cells (less than 30 mm^3) leads to chip-scale optical clocks that are highly desired in satellite communications and navigation systems.[19]

Besides conventional passive optical clocks, active optical clocks, which benefit from the low cavity pulling of the laser oscillation in the bad-cavity limit,[20] have also been demonstrated based on thermal ^{133}Cs atoms[21] and the resulting laser linewidth reached as low as 53 Hz. In the extreme case, the cavity pulling completely vanishes in the cavityless lasing and the laser frequency is entirely determined by the atomic transition.[22,23] Thus, there is no need to reference the laser frequency to an extra high-finesse optical resonator or atomic transition, which substantially reduces the complexity and volume of the clock system and enhances the clock's portability, making active optical clocks promising for out-of-lab and commercial applications. To date, studies on active optical clocks are still in the early stage. Experimentally, only the laser linewidth of active optical clocks has been measured, for example, 53 Hz in Ref. [21] and 1.2 kHz in Ref. [22]. There have been no experimental reports on the frequency stability or accuracy so far. In theory, several works have performed numerical simulations to estimate the frequency stability and accuracy of active optical clocks. For instance, Ref. [24] predicts a frequency stability of $9.3\times10^{-14}/\sqrt{\tau}$, Ref. [25] reports $1.5\times10^{-14}/\sqrt{\tau}$, and Ref. [23] gives a prediction of $3.4\times10^{-14}/\sqrt{\tau}$. Regarding frequency accuracy, Ref. [25] estimates an accuracy level of 10^{-11} for a micro-active optical clock. Although the predicted stability of the 1470 nm active optical clock is two orders of magnitude worse than that of Ramsey–Bordé calcium clocks,[26] it offers a simple architecture, low power consumption, and direct usability of its output as a frequency standard, making it well suited for miniaturized and chip-scale applications. Moreover, its predicted stability is one order of magnitude better than that of MTS-based optical frequency standards, while requiring only a few additional optical components beyond the 459 nm passive clock, presenting a favorable balance between performance and system complexity. In addition, hybridizing chip-scale passive and active optical clocks and a microcomb, where the passive optical clock plays the pumping role for both active optical clock and microcomb and the microcomb is fully stabilized by the two clocks, leads to an architecture of on-chip quantum metrology.[24] Employing a passive optical clock to pump an active optical clock not only creates a compact clock system that can produce multi-wavelength optical frequency standards but also suppresses the influence of the pump noise on the active optical clock.

This work is primarily dedicated to the development of a 459 nm passive optical clock, with a preliminary exploration of the 1470 nm active optical clock. We use two methods, MTS based on the four-wave mixing in a two-level atomic system[27,28] and frequency modulation spectroscopy (FMS) based on the optical heterodyne detection of carrier and sidebands that experience different transmission functions through atoms,[29] to stabilize a 459 nm passive optical clock that also serves as the pump of a 1470 nm active optical clock. We evaluate the effectiveness of MTS and FMS as frequency references for the stabilized pump source of a 1470 nm active optical clock. The MTS method achieves a short-term Allan deviation between two independent frequency-locked 459 nm lasers of $3.7\times10^{-13}/\sqrt{\tau}$ (that is, $2.6\times10^{-13}/\sqrt{\tau}$ for each clock). In contrast, the MTS-FMS beat-note measurement yields a frequency stability of $6.4\times10^{-13}/\sqrt{\tau}$, which is worse than that of the MTS-MTS beat note due to the residual amplitude modulation (RAM).[29] We further use the locked 459 nm passive optical clock to drive a 1470 nm cavityless laser and obtain an output power over 10 μW. The pump-beam-induced light shift of the 1470 nm laser transition is estimated to be $2\pi\times11$ Hz and the uncertainty caused by the pump-power fluctuations is as low as $2\pi\times0.5$ mHz (fractional uncertainty of 2.4×10^{-18}).

2. Physical system

Figure 1(a) illustrates the frequency-stabilization schematic of the 459 nm passive optical clock whose frequency is referenced to the $6S_{1/2}$–$7P_{1/2}$ transition in thermal ^{133}Cs atoms (see Fig. 1(b)). The lifetime of $7P_{1/2}$ is 0.17 μs.[30] Two commercial ECDLs (external cavity diode laser) produced by Zhejiang Faraday Laser Technology Company Limited (Faraday Co., Ltd.) serve as the local oscillators of the MTS/FMS-based optical clock, with the second, independent laser introduced for subsequent beat note experiments. The maximum laser power reaches 60 mW and the spectral linewidth is tens of kHz.

The output laser first passes through an optical isolator (Thorlabs IO-3D-780-VLP) to suppress the retro-reflection. It is then split into a P-polarized beam for pumping a 1470 nm active optical clock (see below) and an S-polarized beam for MTS/FMS-based frequency locking using a half-wavelength plate (HWP) and a polarizing beam splitter (PBS). The S-polarized beam is further divided into a pump beam and a

probe beam via another HWP-PBS combination. Approximately 2.7 mW of the S-polarized light is allocated for the MTS/FMS-based frequency stabilization. This beam is further split into a probe beam (0.32 mW) and a pump beam (1.5 mW). The probe beam passes through a ϕ25 mm×75 mm cylindrical glass cell containing thermal ^{133}Cs atoms and is subsequently detected by a photodetector (PD, Thorlabs PDA10CS2).

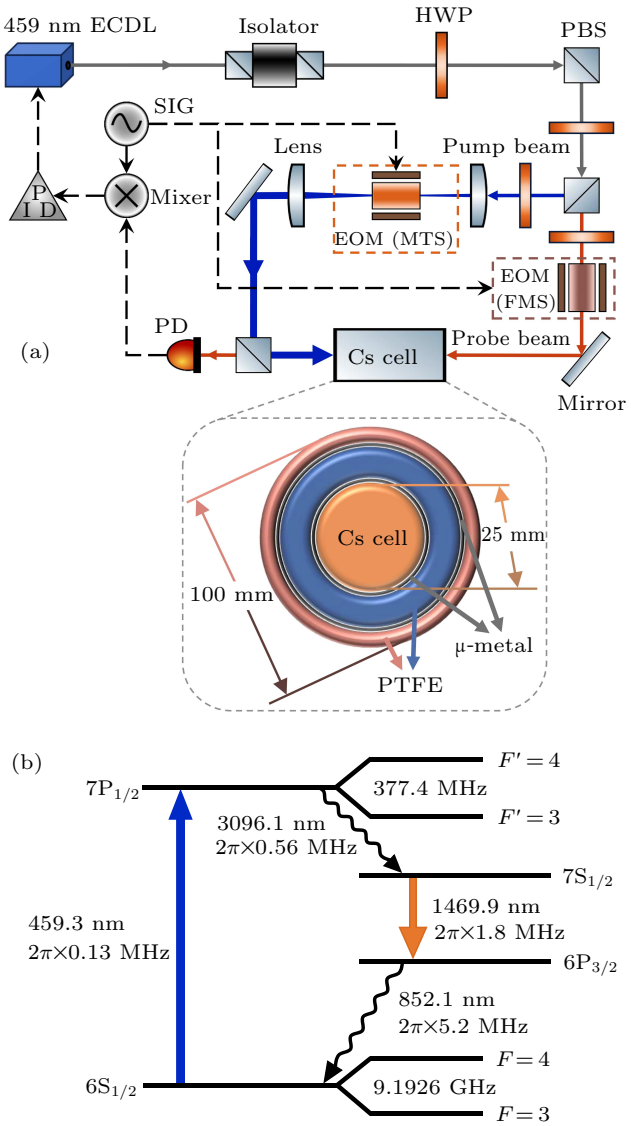


Fig. 1. (a) Schematic of 459 nm passive optical clock. The MTS-EOM is located in the pump beam path and the FMS-EOM is positioned in the probe beam path. ECDL, external cavity diode laser; HWP, half-wave plate; PBS, polarizing beam splitter; PD, photodetector; SIG, signal generator; PID, proportion-integral-derivative locking system. The lower subfigure shows the structure of thermal insulation (polytetrafluoroethylene, PTFE) and magnetic shielding (μ-metal) for the ^{133}Cs vapor cell. (b) Energy level structure of ^{133}Cs. The 459 nm passive optical clock is referenced to the $6S_{1/2}(F = 4)$–$7P_{1/2}$ atomic transition. The population inversion occurs between the $7S_{1/2}$ and $6P_{3/2}$ levels, serving as the laser transition for the 1470 nm active optical clock. Spontaneous decay channels are marked by wavy lines with arrows.

Precise temperature control and magnetic shielding of the atomic vapor cell are critical measures to ensure frequency stability and accuracy. Temperature fluctuations directly affect the vapor density and thermal motion of atoms, leading to variations in Doppler and collision shifts. External magnetic fields (e.g., Earth's field and electronic interference) alter atomic energy levels via the Zeeman effect. To address these issues, we designed the multilayer structure of the ^{133}Cs vapor cell as shown in Fig. 1(a). The cell is heated using tightly wound constantan wire in a bifilar configuration to avoid generating additional magnetic fields. A commercial temperature controller, which is coupled with a PT100 thermistor, monitors and regulates the cell temperature by adjusting the heater current accordingly.

A multilayer structure of thermal insulation and magnetic shielding is implemented outside the heating layer. The thermal insulation consists of two concentric polytetrafluoroethylene (PTFE) cylinders with inner/outer diameters of 40/70 mm and 80/100 mm, respectively, and a length of 200 mm. For magnetic shielding, we employ two layers of heat-treated, demagnetized μ-metal (thickness of 0.2 mm and length of 200 mm) placed inside the insulating cylinders to substantially suppress external transverse and axial magnetic fields. Measurements under steady-state conditions show that the temperature fluctuation of the vapor cell remains below 3 mK over approximately one-minute intervals, while the residual magnetic field inside is at the level of 1 mG.

The optical path difference between MTS and FMS lies in the position of their EOMs because of their distinct physical mechanisms. The MTS-EOM is located in the pump beam path, where two lenses are placed on either side of the EOM to expand the pump beam diameter by a factor of two. In contrast, the FMS-EOM is positioned in the probe beam path, where the modulation signal is directly imposed on the probe beam. In both cases, an HWP is placed before the EOM to align the polarization direction of the beam with the principal axis of the EOM crystal, thereby maximizing modulation efficiency.

The probe beam incident upon the PD is converted into an electrical signal and subsequently divided into two components, SAS (saturated absorption spectroscopy) and MTS/FMS signals. The SAS signal is directly displayed on the oscilloscope. The MTS/FMS component undergoes filtering via a high-pass filter (Mini-Circuits, ZFHP-1R2-S+) and a low-pass filter (Mini-Circuits, BLP-1.9+), followed by amplification using a low-noise amplifier (Mini-Circuits, ZFL-500LN+). The filtered signal is then demodulated using a mixer (Mini-Circuits, ZLW-6+), yielding the error signal. Finally, the error signal is sent into a proportional-integral-derivative (PID) controller (produced by Faraday Co., Ltd.) to adjust the injection current of the diode laser, thus locking the laser frequency to the atomic transition.

3. MTS-stabilized 459 nm optical clock

MTS builds upon SAS by transferring modulation sidebands onto the absorption spectral lines of atoms, yielding narrow-linewidth spectroscopy. Compared with conventional SAS, MTS possesses the advantages of zero background, high signal-to-noise ratio (SNR), minimal frequency drift, and steep response slope. In MTS, a frequency-modulated strong (pump) beam passes through a resonant gaseous medium, where a frequency-unmodulated weak (probe) beam propagates in the opposite direction and collinear to the pump beam (see Fig. 1(a)). The four-wave mixing dominates the nonlinear interaction between two beams and the medium.[27,28] For example, the pump's carrier and one of its sidebands interact with the probe beam via the medium's third-order susceptibility, generating a fourth (phase-conjugate) wave that acts as a sideband to the probe beam (i.e., inducing the frequency modulation of the probe beam). The interference between this new wave and the strong pump beam produces a detectable signal.

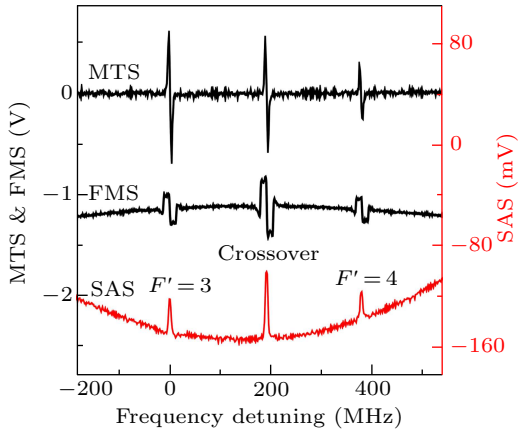


Fig. 2. MTS, FMS and SAS of the $6S_{1/2}(F=4)$–$7P_{1/2}(F'=3,4)$ hyperfine transitions in ^{133}Cs. The frequency separation between the $F'=3$ and $F'=4$ transitions approximates $2\pi\times 377.4$ MHz. For MTS and SAS, the cell temperature is 110 °C and the modulation frequency is $2\pi\times 1.53$ MHz. For FMS, the cell temperature is 120 °C and the modulation frequency is $2\pi\times 25$ MHz.

We measure SAS and MTS of the $6S_{1/2}(F=4)$–$7P_{1/2}(F'=3,4)$ hyperfine transitions in ^{133}Cs (see Fig. 2). SAS presents one crossover resonance, which arises from the velocity-selective Doppler compensation in atoms with nonzero axial velocity components, and two side absorption spikes, which respectively correspond to the $F'=3$ and $F'=4$ hyperfine transitions. The frequency separation between the crossover and either side peaks approximates $2\pi\times$ 188.8 MHz.[31] In contrast, the MTS signal exhibits a dispersive behavior around each SAS spike and its amplitude and zero-crossing slope are maximized around the $F'=3$ transition, beneficial to the laser frequency stabilization. A steep slope provides a high SNR to the frequency locking. Additionally, the MTS profile is closely related to the phase difference between the modulation signal applied on EOM and the demodulation signal fed into the mixer (see Fig. 1(a)). As illustrated in Fig. 3, the out-of-phase MTS may have multiple zero crossings and the slope at the central zero crossing is reduced compared to that of the in-phase MTS. Such lineshape variations highlight the importance of the phase alignment in achieving optimal measurement conditions. In what follows, we use the in-phase MTS of the $6S_{1/2}(F=4)$–$7P_{1/2}(F'=3)$ hyperfine transition to stabilize the 459 nm optical clock.

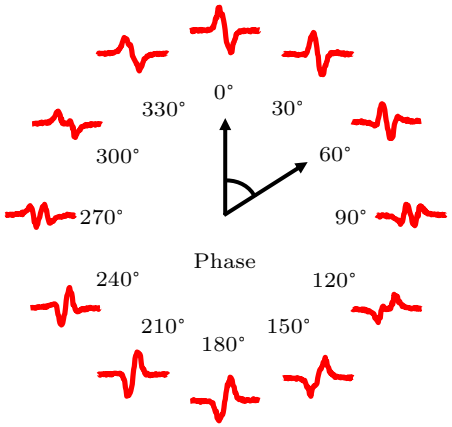


Fig. 3. Dependence of the measured MTS lineshape on the phase difference between modulation and demodulation signals. The cell temperature is 110 °C and the modulation frequency is $2\pi\times 1.53$ MHz. In experiment, the sinusoidal modulation (demodulation) signal has a peak-to-peak voltage of 6 V (1 V).

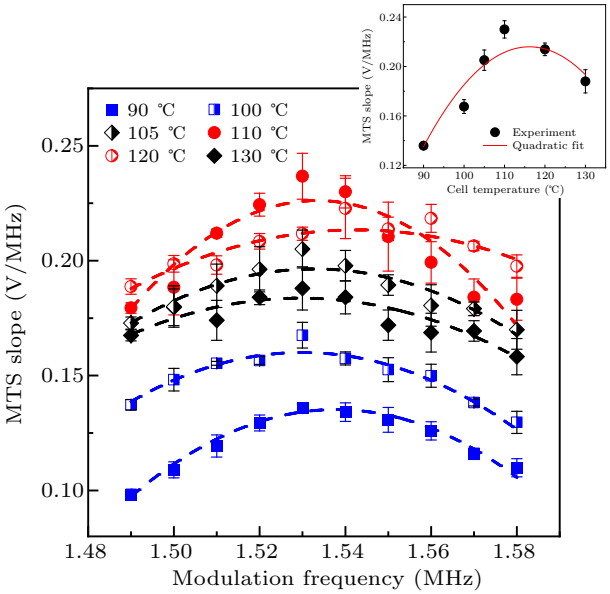


Fig. 4. Slope of the error signal at zero-crossing (obtained from linear fitting) for MTS under different modulation frequencies and temperatures (inset). Each data point corresponds to an average of fifteen measurements. Error bars denote standard deviations. Curves result from the polynomial fit. The optimal operating point of the 459 nm optical clock is set at the cell temperature of 110 °C and the modulation frequency of $2\pi\times 1.53$ MHz.

The zero-crossing slope of MTS determines the sensitivity to frequency fluctuations. We measure the slope at different cell temperatures and EOM modulation frequencies so as to identify the optimal operating point of the clock system. The results have been summarized in Fig. 4. As the modulation

frequency is increased, the MTS slope experiences an initial increase followed by a decrease and a pronounced enhancement can be observed around $2\pi \times 1.53$ MHz. The spectral linewidth of the $6S_{1/2}(F=4)$–$7P_{1/2}(F'=3)$ hyperfine transition is measured to be $2\pi \times 6.9$ MHz from the data plot, greatly exceeding the natural linewidth due to the saturation broadening.[32] The broadening effects should be taken into account when interpreting spectroscopic data and optimizing system performance. The optimal modulation frequency is approximately 0.22 times the measured linewidth, consistent with the result in Ref. [16]. This empirical ratio may provide a practical guide for setting up similar MTS-based systems. We vary the cell temperature between 90 °C and 130 °C and find that the slope is maximized around 110 °C. The optimization of temperature balances the atomic density and the spectral broadening to achieve an optimal signal quality.

After identifying the optimal operating condition, we lock the frequency of 459 nm optical clock to the $6S_{1/2}(F=4)$–$7P_{1/2}(F'=3)$ hyperfine transition. To evaluate the clock stability, we perform the beat note between two MTS-stabilized clocks under the same experimental conditions, where, however, the other laser system is referenced to the crossover resonance. The beat signal at the frequency of $2\pi \times 188.8$ MHz is measured over several hours by a high-bandwidth photodetector (Hamamatsu C5658, bandwidth of $2\pi \times 1$ GHz) in the free space and is monitored by a spectrum analyzer (Keysight N9002B). The recorded spectrum is slightly narrower than that of the beat note between two free-running lasers. The FWHM (full width at half maximum) of the latter is derived to be $2\pi \times 30.6$ kHz through the Lorentzian fitting (see Fig. 5(a)). That is, the linewidth of commercial ECDLs produced by Faraday Co., Ltd. may reach tens of kHz. Thus, the intrinsic noise of lasers, approaching fundamental technical limits, prevents substantial further linewidth reduction through MTS stabilization.[33]

The beat-note frequency is recorded using a frequency counter (Keysight 53230A) and the corresponding Allan deviation $\sigma_y(\tau)$ is evaluated accordingly. As shown in Fig. 5(b), $\sigma_y(\tau)$ for two free-running lasers is always above 6×10^{-11} and suffers the frequency drift after $\tau > 0.1$ s because of temperature fluctuations. In contrast, the relative short-term stability between two MTS-stabilized clocks follows $\sigma_y(\tau) = 3.7 \times 10^{-13}/\sqrt{\tau}$ for $\tau < 1$ s. Assuming equal contributions from both clocks, the frequency stability of individual clocks is inferred to be $2.6 \times 10^{-13}/\sqrt{\tau}$, better than that of the 778 nm optical clock based on the $5S_{1/2}$–$5P_{3/2}$–$5D_{5/2}$ two-photon transition in thermal ^{87}Rb atoms.[15]

In addition, the observed increase in Allan deviation around $\tau \approx 1$ s can be attributed to the combined effects of several physical limitations in the system. The thermal control system, constrained by its finite response time, cannot fully suppress short-timescale temperature fluctuations. These fluctuations directly modulate the cesium vapor density, inducing frequency shifts through atom–atom collisions. The key mechanism in vapor-cell atomic clocks is that thermal atom collisions cause density-dependent energy level shifts tightly linked to cell temperature. Mapping such temperature fluctuations onto the reference transition frequency introduces clock instability. Based on the measured clock stability of 2.6×10^{-13}, we infer the collision shift coefficient to be $2\pi \times 3.4$ kHz/K, consistent with results in Ref. [16].

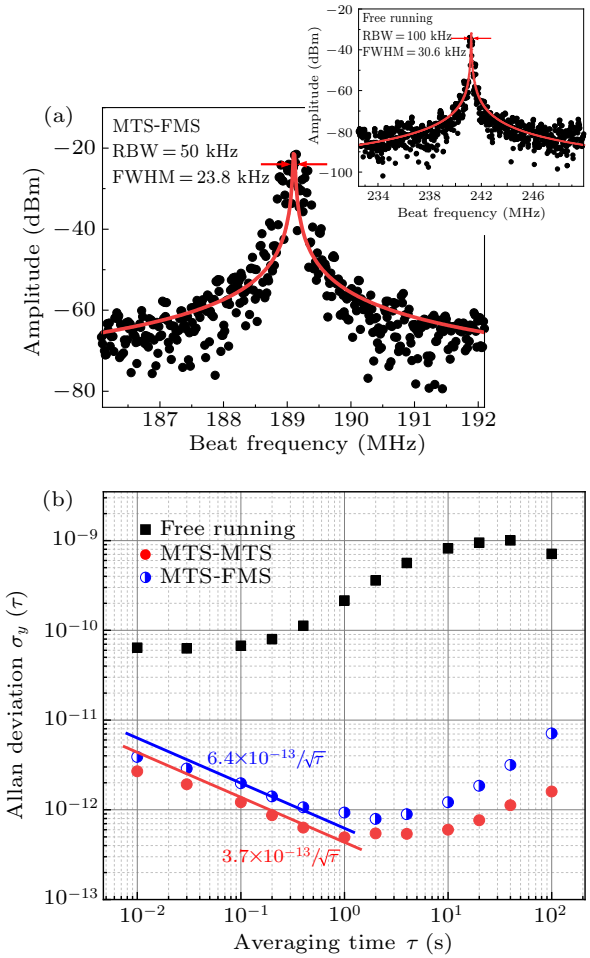


Fig. 5. Beat note between two stabilized 459 nm optical clocks. (a) Spectrum of beat note between MTS- and FMS-stabilized 459 nm lasers with a Lorentz-fitted FWHM of $2\pi \times 23.8$ kHz. Inset: spectrum of beat note between two free-running lasers with a FWHM of $2\pi \times 30.6$ kHz. (b) Allan deviation of beat note between two optical clocks. Squares: two free-running lasers. Filled circles: two MTS-stabilized clocks. Semi-hollow circles: MTS- vs. FMS-stabilized clocks. Lines: curve fitting.

Compounding this effect, the servo loop for laser frequency stabilization exhibits insufficient gain in the low-frequency regime, limiting its ability to suppress slow technical noise sources such as thermal drift and electronic instabilities that further contribute to frequency fluctuations.

External magnetic field effects also play a role. Despite the use of a two-layer μ-metal magnetic shield, residual magnetic field fluctuations (on the order of mG) still affect the atomic transition frequency. According to the Breit–Rabi

formula,[34,35] the $6S_{1/2}(F=4)$ ground state experiences a quadratic Zeeman shift scaling with the square of the magnetic field strength. In contrast, the Zeeman shift of the $m_{F'}=0$ sublevel in the $6S_{1/2}(F=4)$ excited state remains relatively small compared to typical hyperfine intervals.[36] With a residual magnetic field of a few mG in experiments, the combined Zeeman shift of the reference transition can reach tens of Hz; assuming a 10% uncertainty in the magnetic field, the resulting instability from the Zeeman effect is estimated at the 10^{-15} level. Implementing active magnetic field compensation could help mitigate this contribution. [37]

We also measure the power stability of the MTS-stabilized 459 nm optical clock since it may serve as the pump for a 1470 nm active optical clock and causes the light shift of the 1470 nm laser transition (see below). As shown in Fig. 6, the Allan deviation goes down when the averaging time τ is less than 4 s and reaches a minimum of 3.6×10^{-5}. The power drift remains at the 10^{-5} level for up to 60 s. Further improvement of power stability can be implemented using a power stabilization device and the potential stability reaches the 10^{-7} level.[38]

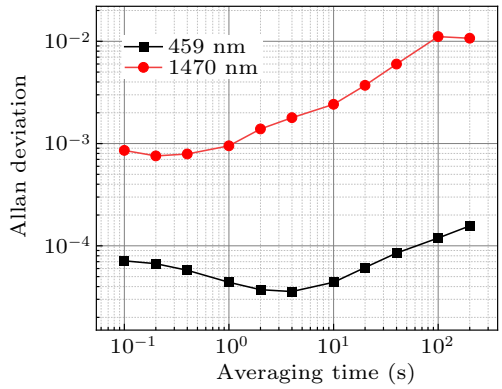


Fig. 6. Power stability of MTS-stabilized 459 nm laser and 1470 nm laser. MTS modulation frequency: $2\pi\times1.53$ MHz; MTS cell temperature: 110 °C. The 459 nm laser (pump source for the 1470 nm laser) is locked to the ^{133}Cs $6S_{1/2}(F=4)$–$7P_{1/2}(F'=3)$ hyperfine transition (pump power: 22.3 mW, 1470 nm cell temperature: 105 °C).

4. FMS-stabilized 459 nm optical clock

In addition to MTS, FMS is also a widely used high-resolution laser spectroscopic technique with the advantages of enhanced sensitivity and noise immunity.[29,39,40] By shifting the detection bandwidth to a frequency regime much higher than the FWHM of the atomic reference transition, FMS effectively suppresses low-frequency technical noise, thus significantly improving SNR. In the field of optical clocks, FMS provides a reliable means to stabilize laser frequency by detecting dispersive features near atomic resonances. In this section, we employ FMS to lock a 459 nm laser to the crossover resonance in thermal ^{133}Cs atoms and assess the performance of the resulting optical clock.

In FMS, an EOM is used to sinusoidally modulate the frequency of the probe beam at a frequency (typically, tens to hundreds MHz) much exceeding the spectral linewidth of the atomic transition, allowing for the separation from the low-frequency technical noise. The carrier and two sidebands experience different transmission amplitudes when passing through the atomic vapor that is saturated by a strong pump beam. This frequency-dependent interaction of each spectral component with the atomic resonance profile imprints the derivative of the absorption spectrum, typically the first derivative, on the transmitted signal.[41] A lock-in amplifier then demodulates the signal at the modulation frequency, extracting a dispersive error signal that is used for the laser frequency stabilization.

The experimental setup of FMS differs from that of MTS primarily in the placement of the EOM, where the FMS-EOM is positioned in the probe beam path (see Fig. 1(a)). We measure the FMS signal of the $6S_{1/2}(F=4)$–$7P_{1/2}(F'=3,4)$ hyperfine transitions (see Fig. 2). The measurements are carried out under optimized pump and probe powers to maximize the SNR while avoiding power broadening effects. Compared to MTS, FMS clearly exhibits a nonzero background, which is mainly caused by RAM and imperfect demodulation. These imperfections are often attributed to factors such as EOM bias drift, temperature fluctuations, and variations in the polarization state of the optical beam. The presence of this background may shift the zero-crossing point of the error signal when the laser power and modulation conditions are changed, thereby introducing additional uncertainty into the frequency locking.

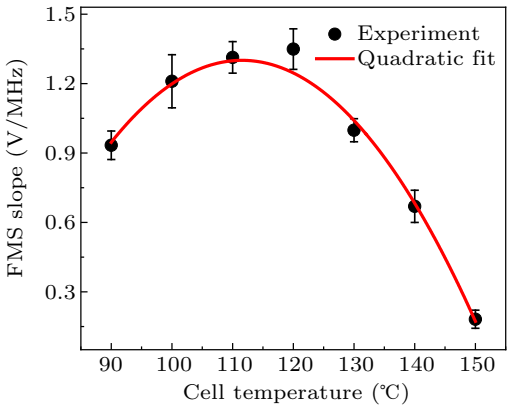


Fig. 7. Slope of the error signal at zero-crossing (determined by linear fit) vs. cell temperature at a modulation frequency of $2\pi\times25$ MHz. Each point represents an average of 10 measurements. Error bars indicate the standard deviation. The curve results from a polynomial fit. The optimal operating temperature for FMS is determined to be 120 °C.

Due to the limitations of the signal generator, the modulation frequency of the EOM is set to be $2\pi\times25$ MHz, which is sufficient for FMS experiments, since the theory predicts that the FMS slope hardly changes when the modulation frequency exceeds $2\pi\times15$ MHz.[29] In practice, setting the modulation frequency moderately above this threshold ensures both effective noise suppression and a well-defined dispersive signal (see Fig. 2). Figure 7 illustrates the dependence of the FMS slope

(corresponding to the crossover resonance) on the cell temperature. The slope increases with temperature and reaches a maximum around 120 °C, indicating an optimal balance between atomic density and Doppler broadening.

To evaluate the frequency stability of the FMS-stabilized 459 nm laser, we conduct a heterodyne beat measurement between the MTS- and FMS-stabilized lasers over a duration exceeding two hours. The resulting beat note, depicted in Fig. 5(a), displays a Lorentzian lineshape with a FWHM of $2\pi \times 23.8$ kHz, closely matching the linewidth observed in the MTS-MTS beat note. This similarity indicates comparable spectral purity between the two stabilization methods. The corresponding Allan deviation of the beat note frequency is presented in Fig. 5(b). For a sampling time less than 1 s, the Allan deviation follows $6.4 \times 10^{-13}/\sqrt{\tau}$, implying a single-clock stability of $4.5 \times 10^{-13}/\sqrt{\tau}$ under the assumption of equal contribution from both systems. Compared to the MTS-MTS beat note, the FMS-MTS beat note produces a higher short-term instability, which is primarily attributed to the residual amplitude modulation and imperfect signal symmetry inherent to the FMS technique.

5. MTS- vs. FMS-based frequency stabilization

The observed Allan deviation and the narrow beat-note linewidth (23.8 kHz FWHM in Fig. 5(a)) clearly demonstrate the efficacy of MTS in stabilizing laser frequency. Compared to the MTS-FMS scheme, the MTS-MTS locking exhibits markedly superior short-term frequency stability (filled circle data in Fig. 5(b)), which is attributed to its intrinsic immunity to RAM and a high SNR in dispersion. The modestly reduced performance observed in the MTS-FMS configuration (semi-hollow circle data in Fig. 5(b)) may result from the RAM-induced nonzero background (Fig. 2). These results manifest MTS as a robust and reliable technique for applications requiring narrow linewidths and stable laser frequencies, including quantum optics and precision metrology.

While the detailed operational principles of MTS and FMS have been presented in Sections 3 and 4, respectively, here we focus on comparing their performance characteristics and practical implications for the frequency stabilization. The MTS technique demonstrates better short-term frequency stability, as evidenced by a lower Allan deviation and narrower beat-note linewidth. This advantage stems from its intrinsic suppression of RAM and background-free signal profile, which contribute to a higher SNR and improved locking precision. In contrast, FMS provides a simpler experimental setup and faster response time but suffers from a nonzero baseline in its error signal due to RAM and imperfect demodulation, leading to a reduced stability. When considering the low-order modulation, the RAM is proportional to the light intensity.[42] Additionally, the locking point in FMS is more sensitive to the variations in the laser power and modulation conditions, which can introduce the long-term frequency drift. Therefore, for the applications requiring high frequency stability and low noise, MTS is generally the preferred choice, whereas FMS may be suitable for compact and rapid detection scenarios where the system simplicity is prioritized.

Moreover, in practical optical clock systems, the trade-off between performance and complexity must be carefully considered. Although MTS typically involves more elaborate beam alignment and modulation configurations, its superior locking quality justifies the added system complexity for high-precision applications. On the other hand, FMS, despite its slightly inferior stability, remains a valuable method in scenarios that demand simpler setups and reduced component count.

Compared with the existing 1560–780 nm optical clock based on the $5S_{1/2}$–$5P_{3/2}$–$5D_{5/2}$ two-photon transition in rubidium,[15] our MTS-stabilized 459 nm optical clock offers several advantages, including the higher SNR due to its single-photon transition scheme and the simpler system architecture without the need for frequency doubling. Such merits enhance both compactness and reliability of the optical clock, providing a feasible route toward future miniaturized and integrated optical frequency standards.

6. The 1470 nm laser

The 459 nm passive optical clock can be used to pump a 1470 nm active optical clock (i.e., a laser system that is operated in the bad-cavity limit[21]). The concept of active optical clocks[20] has recently been proposed as a means to substantially reduce the influence of cavity noise (Brownian thermal noise[43]) on the laser frequency stability by orders of magnitude. As a result, the laser frequency may directly serve as an optical frequency standard without the need of an extra frequency locking loop. Next, we construct a cavityless 1470 nm laser and conduct preliminary experimental investigations on active optical clocks.

The 1470 nm laser is built upon a four-level scheme in ^{133}Cs (see Fig. 1(a)). Here, a 459 nm pump laser excites atoms from the $6S_{1/2}$ ground state to the $7P_{1/2}$ excited state. The atoms then spontaneously decay to $7S_{1/2}$, followed by the stimulated transition to $6P_{3/2}$, during which photons at 1470 nm are emitted. In the absence of a conventional optical cavity, i.e., cavityless, the system relies on amplified spontaneous emission and partially stimulated emission to achieve lasing.[22,23] Although a traditional feedback cavity is not used, a partially reflective mirror (such as a high-reflectivity mirror for 1470 nm) is utilized to introduce a weak optical feedback, thereby enhancing the directional amplification process and enabling quasi-laser emission.

The experimental setup is illustrated in Fig. 8(a). The 459 nm optical clock provides the pump power to a ^{133}Cs va-

por cell whose length is 7.5 cm. The cell is heated to 105 °C or 115 °C using an external heater. The M1 concave mirror has a radius of curvature of 250 mm and is coated for high reflectivity (99.7%) at 1470 nm and anti-reflection (10%) at 459 nm. A dichroic optical filter is used to block the 459 nm pump light while transmitting the generated 1470 nm light. The PD1 and PD2 commercial photodetectors are used to monitor the 1470 nm power and SAS (for reference), respectively. An adjustable iris diaphragm is utilized to control the beam size. The optimal photodetector signal is obtained when the beam spot diameter is adjusted to 1 mm.

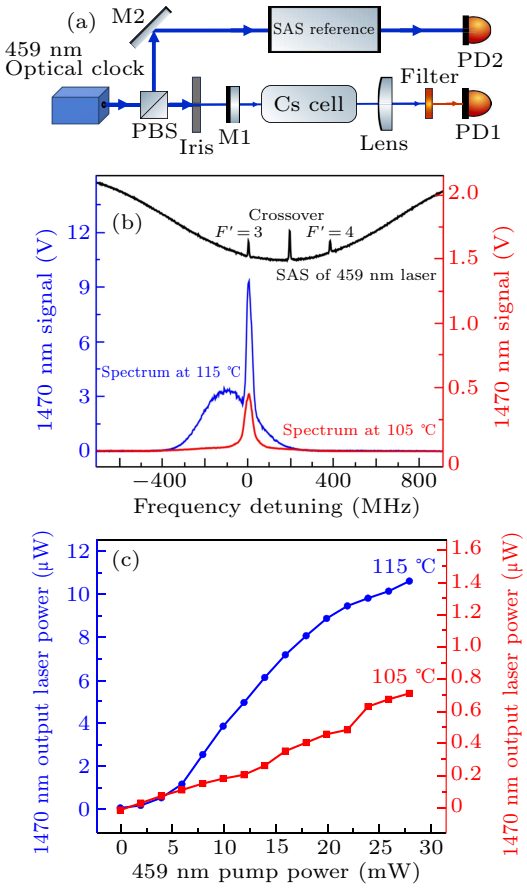


Fig. 8. (a) Experimental setup of 1470 nm cavityless laser. The M1 concave mirror has a high transmittance of 459 nm and a high reflectivity of 1470 nm. The filter only allows the 1470 nm laser light to pass through. (b) Resonance spectrum of the 1470 nm laser when sweeping the 459 nm laser frequency. The x axis stands for the 459 nm frequency. SAS signal as the reference for the MTS-locked 459 nm laser. The upper curve is the 459 nm saturated absorption spectroscopy corresponding to the $6S_{1/2}(F=4)$–$7P_{1/2}$ transition. The middle curve is the 1470 nm resonance spectrum at 115 °C with a 459 nm laser power of 22.3 mW. The lower curve is the 1470 nm resonance spectrum at 105 °C with the same pump power. (c) Threshold curves of 1470 nm laser at 105 °C and 115 °C. The 459 nm laser is resonant to the $6S_{1/2}(F=4)$–$7P_{1/2}$ atomic transition.

Figure 8(b) presents the measured 1470 nm output spectrum as the frequency of the 459 nm optical clock is scanned across the $6S_{1/2}(F=4)$–$7P_{1/2}(F'=3)$ transition. The SAS provides a reference transition profile against which the MTS lock point is verified. At a cell temperature of 105 °C, a weak 1470 nm emission is observed. The 1470 nm output power exhibits a linear growth as the pump power is increased (see Fig. 8(c)). In contrast, at 115 °C, the elevated atomic density due to the increased temperature leads to a pronounced spectral peak plus a strong background fluorescence at 1470 nm. A distinct lasing threshold behavior emerges at 1470 nm as the pump power increases, with the measured threshold occurring at approximately 5 mW of 459 nm pump power, confirming the observation of cavityless lasing.

Direct measurement of the absolute frequency and spectral linewidth of the 1470 nm laser is currently precluded by limitations in our experimental setup. Nevertheless, in addition to demonstrating 1470 nm cavityless laser, we also quantitatively evaluate the 459-nm-pump-induced frequency shift of the $6P_{3/2}$–$7S_{1/2}$ laser transition in ^{133}Cs. Since the pump frequency is nearly three times higher than that of the 1470 nm transition, the resulting light shift is significantly suppressed. We have characterized the power stability of the 459 nm pump laser and 1470 nm laser in Fig. 6. At 1470 nm laser output powers exceeding 10 μW, the power Allan deviation is 9.5×10^{-4} at $\tau=1$ s. The pump-beam intensity inside the vapor cell (for the generation of the 1470 nm laser) is 28.4 mW/mm^2 and the induced ac Stark shift of the $6P_{3/2}$–$7S_{1/2}$ transition is calculated to be $2\pi\times11$ Hz.[23] Thus, the uncertainty arising from pump power fluctuations is estimated to be $2\pi\times0.5$ mHz (fractional uncertainty of 2.4×10^{-18}). To date, no experimental measurement of the stability or accuracy of the 1470 nm clock has been reported, but we anticipate that achieving a stability level better than 10^{-18} will be extremely challenging. Therefore, we believe that the power fluctuations of the 459 nm passive optical clock have a negligible influence on the 1470 nm active optical clock.

7. Conclusion

In this work, we have demonstrated a 459 nm passive optical clock based on the $6S_{1/2}(F=4)$–$7P_{1/2}(F'=3)$ transition in thermal ^{133}Cs atoms, utilizing both MTS and FMS techniques. Through systematic optimization of modulation frequency, vapor cell temperature, and system configuration, the MTS scheme achieved a short-term frequency stability of $2.6\times10^{-13}/\sqrt{\tau}$, outperforming that of the FMS-based system ($4.5\times10^{-13}/\sqrt{\tau}$). The superior performance of MTS stems from its intrinsic immunity to RAM and higher SNR, as confirmed by beat-note linewidth measurements and Allan deviation analysis. In contrast, FMS, while simpler in configuration, exhibits a slightly degraded stability due to RAM-induced background offsets and lower signal symmetry compared to MTS.

Currently, the long-term stability of the 459 nm clock is primarily limited by residual temperature fluctuations of the vapor cell, imperfect magnetic shielding, and low-frequency technical noise. These factors degrade the frequency stability

beyond 1 s averaging time. In future work, the implementation of active thermal control with shorter response time, active magnetic field compensation, and low-noise electronics is expected to suppress these instabilities. With such improvements, it is anticipated that the long-term frequency stability may follow the level of $3.7 \times 10^{-13}/\sqrt{\tau}$ at $\tau = 10$ s.

Besides the realization of a stable 459 nm passive optical clock, we also demonstrate its practical utility as a pump source for a cavityless 1470 nm active optical clock, based on a four-level lasing scheme in ^{133}Cs vapor. The 1470 nm output power exceeds 10 μW and a clear lasing threshold behavior is observed, confirming the feasibility of cavityless lasing in this configuration. This hybrid approach not only enables compact multi-wavelength frequency standards but also reduces cavity noise and simplifies the system architecture. Looking forward, further optimization of the 1470 nm active optical clock, particularly in terms of frequency stability and output power, will be essential for advancing toward integrated and chip-scale applications.

Our work demonstrates a promising route toward miniaturized, multi-wavelength optical clocks that combine the benefits of both passive and active schemes. The potential integration of such hybrid systems with stabilized optical frequency microcombs may open new avenues in chip-scale quantum metrology, frequency networking, and portable high-precision timekeeping devices. These advances hold significance for out-of-laboratory applications, including satellite navigation, fundamental physics tests, and resilient timing in complex environments.

Acknowledgements

D.Y. acknowledges the funding provided by CAS Project for Young Scientists in Basic Research (Grant No. YSBR-085) and National Time Service Center (Grant No. E239SC1101). Z.L. thanks the funding of Wenzhou Major Science & Technology Innovation Key Project (Grant No. ZG2023021). J.C. is supported by Innovation Program for Quantum Science and Technology (Grant No. 2021ZD0303200).

References

[1] Nicholson T L, Campbell S L, Hutson R B, Marti G E, Bloom B J, McNally R L, Zhang W, Barrett M D, Safronova M S, Strouse G F, Tew W L and Ye J 2015 *Nat. Commun.* **6** 6896
[2] Aeppli A, Kim K, Warfield W, Safronova M S and Ye J 2020 *Phys. Rev. Lett.* **133** 023401
[3] Dimarcq N, Gertsvolf M, Mileti G, *et al.* 2024 *Metrologia.* **61** 012001
[4] Meiser D, Ye J, Carlson D R and Holland M J 2009 *Phys. Rev. Lett.* **102** 163601
[5] Ushijima I, Takamoto M and Katori H 2018 *Phys. Rev. Lett.* **121** 263202
[6] Nemitz N, Jørgensen A A, Yanagimoto R, Bregolin F and Katori H 2019 *Phys. Rev. A* **99** 033424
[7] Aeppli A, Chu A, Bothwell T, Kennedy C J, Kedar D, He P, Rey A M and Ye J 2022 *Sci. Adv.* **8** eadc9242
[8] Hutson R B, Goban A, Marti G E, Sonderhouse L, Sanner C and Ye J 2019 *Phys. Rev. Lett.* **123** 123401
[9] Brewer S M, Chen J S, Hankin A M, Clements E R, Chou C W, Wineland D J, Hume D B and Leibrandt D R 2019 *Phys. Rev. Lett.* **123** 033201
[10] Takamoto M, Takano T and Katori H 2011 *Nat. Photon.* **5** 288
[11] Bothwell T, Kennedy C J, Aeppli A, Kedar D, Robinson J M, Oelker E, Staron A and Ye J 2022 *Nature* **602** 420
[12] Liu D, Cao J, Yuan J, Cui K, Yuan Y, Zhang P, Chao S, Shu H and Huang X 2023 *Chin. Phys. B* **32** 010601
[13] Pedrozo-Peñafiel E, Colombo S, Shu C, Adiyatullin A F, Zeyang L, Mendez E, Braverman B, Kawasaki A, Akamatsu D, Xiao Y and Vuletić V 2020 *Nature* **588** 414
[14] Robinson J M, Miklos M, Tso Y M, Kennedy C J, Bothwell T, Kedar D, Thompson J K and Ye J 2024 *Nat. Phys.* **20** 208
[15] Martin K W, Phelps G, Lemke N D, Bigelow M S, Stuhl B, Wojcik M, Holt M, Coddington I, Bishop M W and Burke J H 2018 *Phys. Rev. Appl.* **9** 014019
[16] Miao J, Shi T, Zhang J and Chen J 2022 *Phys. Rev. Appl.* **18** 024034
[17] Cheng F, Ning J, Zhang F, Li H, Du Y, Zhang J, Deng K and Lu Z 2021 *Chin. Phys. B* **30** 050603
[18] Miao J, Chen J, Yu D, Yang Q, Pan D and Chen J 2025 *Photon. Res.* **13** 721
[19] Newman Z L, Maurice V, Drake T, Stone J R, *et al.* 2019 *Optica* **6** 680
[20] Chen J 2009 *Chin. Sci. Bull.* **54** 348
[21] Shi T, Pan D and Chen J 2019 *Opt. Express* **27** 22040
[22] Zhang J, Shi T, Miao J, Yu D and Chen J 2024 *npj Quantum Inf.* **10** 87
[23] Yu D, Zhang J, Zhang S and Chen J 2024 *Adv. Quantum Technol.* **7** 2300308
[24] Yu D, Vollmer F, Del'Haye P and Zhang S 2023 *Opt. Express* **31** 6228
[25] Yu D, Vollmer F and Zhang S 2023 *Quantum Sci. Technol.* **8** 025005
[26] Olson J, Fox R W, Fortier T M, Sheerin T F, Brown R C, Leopardi H, Stoner R E, Oates C W and Ludlow A D 2019 *Phys. Rev. Lett.* **123** 073202
[27] Bi Z, Ding L and Ma L 1993 *Acta Phys. Sin.* **42** 582 (in Chinese)
[28] Snyder J J, Raj R K, Bloch D and Ducloy M 1980 *Opt. Lett.* **5** 163
[29] Bjorklund G C, Levenson M D, Lenth W and Ortiz C 1983 *Appl. Phys. B* **32** 145
[30] Toh G, Chalus N, Burgess A, Damitz A, Imany P, Leaird D E, Weiner A M, Tanner C E and Elliott D S 2019 *Phys. Rev. A* **100** 052507
[31] Arimondo E, Inguscio M and Violino P 1977 *Rev. Mod. Phys.* **49** 31
[32] Ito N 2000 *Rev. Sci. Instrum.* **71** 2655
[33] Preuschoff T, Schlosser M and Birkl G 2018 *Opt. Express* **26** 24010
[34] Breit G and Rabi I I 1931 *Phys. Rev.* **38** 2082
[35] Lu B and Chang H 2023 *Chin. Phys. B* **32** 013101
[36] Shang H, Zhang T, Miao J, Shi T, Pan D, Zhao X, Wei Q, Yang L and Chen J 2020 *Opt. Express* **28** 6868
[37] Zeng M, Ma Z, Hu R, Zhang B, Hao Y, Zhang H, Huang Y, Guan H and Gao K 2023 *Chin. Phys. B* **32** 110704
[38] Tricot F, Phung D H, Lours M, Guérandel S and de Clercq E 2018 *Rev. Sci. Instrum.* **89** 113112
[39] Moses E I and Tang C L 1977 *Opt. Lett.* **1** 115
[40] Lenth W, Ortiz C and Bjorklund G C 1982 *Opt. Commun.* **41** 369
[41] Silver J A 1992 *Appl. Opt.* **31** 707
[42] Whittaker E A, Shum C M, Grebel H and Lotem H 1988 *J. Opt. Soc. Am. B* **5** 1253
[43] Numata K, Kemery A and Camp J 2004 *Phys. Rev. Lett.* **93** 250602